applied sciences

MDPI

Article

Quasi-Shor Algorithms for Global Benchmarking of Universal Quantum Processors

Genting Dai [1], Kaiyong He [1], Changhao Zhao [1], Yongcheng He [1], Jianshe Liu [1] and Wei Chen [1,2,3,*]

[1] Laboratory of Superconducting Quantum Information Processing, School of Integrated Circuits, Tsinghua University, Beijing 100084, China
[2] Beijing National Research Center for Information Science and Technology, Beijing 100084, China
[3] Beijing Innovation Center for Future Chips, Tsinghua University, Beijing 100084, China
* Correspondence: weichen@tsinghua.edu.cn

Abstract: This work generalizes Shor's algorithm into quasi-Shor algorithms by replacing the modular exponentiation with alternative unitary operations. By using the quantum circuits to generate Bell states as the unitary operations, a specific example called the Bell–Shor algorithm was constructed. The system density matrices in the quantum circuits with four distinct input states were calculated in ideal conditions and illustrated through chromatic graphs to witness the evolution of quantum states in the quantum circuits. For the real part of the density matrices, it was revealed that the number of zero elements dramatically declined to only a few points after the operation of the inverse quantum Fourier transformation. Based on this property, a protocol constituting a pair of error metrics Γ_a and Γ_b is proposed for the global benchmarking of universal quantum processors by looking at the locations of the zero entries and normalized average values of non-zero entries. The protocol has polynomial resource requirements with the scale of the quantum processor. The Bell–Shor algorithm is capable of being a feasible setting for the global benchmarking of universal quantum processors.

Keywords: universal quantum processor; Shor's factoring algorithm; quantum benchmarking

check for updates

Citation: Dai, G.; He, K.; Zhao, C.; He, Y.; Liu, J.; Chen, W. Quasi-Shor Algorithms for Global Benchmarking of Universal Quantum Processors. *Appl. Sci.* **2023**, *13*, 139. https://doi.org/10.3390/app13010139

Academic Editor: Yang Yu

Received: 6 December 2022
Revised: 19 December 2022
Accepted: 19 December 2022
Published: 22 December 2022

Copyright: © 2022 by the authors. Licensee MDPI, Basel, Switzerland. This article is an open access article distributed under the terms and conditions of the Creative Commons Attribution (CC BY) license (https://creativecommons.org/licenses/by/4.0/).

1. Introduction

Building universal quantum computers is a goal in the field of quantum computing [1–11]. Realizing various algorithms, such as the Deutsch algorithm [12,13], Grover algorithm [14], Harrow–Hassidim–Lloyd algorithm [15–18], Shor's algorithm [19–25], and other derivative results [26–30] on the universal quantum computers have led to tremendous challenges for both hardware and software. Being a paradigmatic example, Shor's algorithm provides a kind of method to find the factors of an odd composite integer of L bits using resources that are polynomial in the $O(L)$ bits, and order-finding as the crux of Shor's algorithm is believed to be exponentially hard on classical computers [31,32].

En route to building scalable quantum processors to realize these algorithms, there have been a variety of benchmarking protocols, such as determining the fidelity of quantum gates [33–37], setting a standard benchmark between the expected and realized states based on different quantum devices [38–41], characterizing quantum processors directly for scalability, and robustness [4,42–48]. In addition, some relevant theories calculated for distillation and optimization in quantum sources are proposed [49–52]. The architecture of superconducting quantum processors is the key to its performance, including the number of qubits, computational depth, and the connectivity of different qubits [53–55]. Single-qubit or even two-qubit gate operations could only focus on the properties of superconducting qubits and reduce the emphasis on the interconnection between these qubits [47,53,54,56,57]. Thus, it would be rewarding to carry out global benchmarking focused on the overall performances of small-scale circuits and then scale it to larger sizes. Quantum state tomography (QST) has generally been utilized for presenting the overall performances of quantum processors [58,59]. However, the scalability

of the existing QST protocol could be a major pitfall for the exponential growth in the resource with the scaling of the processor.

To address this problem, we are attempting to cut down the measurement costs of QST by systematically selecting a subset of qubits in the quantum processor. This paper proposes a quasi-Shor algorithm, which replaces the modular exponentiation in Shor's algorithm with other unitary operations, preserves similar frames, and simplifies quantum operations. Taking quantum circuits for generating Bell states as specific examples, a so-called Bell–Shor algorithm was constructed. The Bell–Shor algorithm involves both single-qubit operations and two- or even three-qubit operations together. The evolution of quantum states is calculated during the whole Bell–Shor algorithm and the results of density matrices are visualized as two-dimensional chromatic graphs. The traits of these matrices include the location of the maximum and zero elements. Remarkably, the number of zero elements decreases to a few points in the density matrices after all the processes, which are the heralds of distinguishing features between different input states. Some suitable error metrics are introduced and benchmarking protocols are formulated. Due to the combination of both the single-qubit operations and two-qubit operations on any qubits, the Bell–Shor algorithm is a feasible setting for the global benchmarking of universal quantum processors.

This paper is organized as follows. The circuits of the quasi-Shor and Bell–Shor are introduced in Section 2, which generalizes the structure of the algorithm. In Section 3, density matrices along the route of the circuit are shown, including both the real part and the imaginary part. Two metrics, Γ_a and Γ_b, are discussed in Section 4, in which the locations of the special entries are displayed. Then the conclusion and summary are in Section 5.

2. Quasi-Shor and Bell–Shor Algorithms

Shor's factoring algorithm involves two registers in the quantum processors [19,59]. The first one contains t qubits set in $|0\rangle$ state initially. The t relies on the number of digits of calculated accuracy and the probability of success of the phase estimation process. The second register starts with $|1\rangle$ state, which should have enough qubits to store quantum information.

As shown in Figure 1a, quasi-Shor algorithms replace the modular exponentiation in Shor's algorithm with unitary operations M_i $(i = 1, 2, 3\ldots)$. In the first register, the circuit contains a series of Hadamard gates, which are followed by controlled-M_i. Then inverse quantum Fourier transformation ($\mathrm{QFT}^\dagger$) is applied to the first register. It still holds the analog frame of the quantum circuit with Shor's algorithm. The measurement of all these qubits after $\mathrm{QFT}^\dagger$ could be exploited to benchmark the performance of the quantum processor.

Figure 1b gives the schematic of the Bell–Shor algorithm based on five qubits, which are divided into two registers with three and two qubits, respectively. This combination keeps a certain complexity by retaining three computation periods with three controlling qubits in the first register while simplifying the varieties of entangled states through Bell states with two computing qubits. The quantum operation M is set as a combination of a Hadamard gate and a CNOT gate, which is denoted as a Controlled-Bell (C-Bell) quantum operation:

$$M = \mathrm{CNOT} * (H \otimes I). \tag{1}$$

As a case study, when M_i $(i = 1, 2, 3)$ satisfy $M_i = M^{2^{i-1}}$ $(i = 1, 2, 3)$, the quasi-Shor algorithm could be utilized to complete phase estimation. For further simplification, M_i $(i = 1, 2, 3)$ satisfy $M_i \equiv M$ $(i = 1, 2, 3)$, the brief quantum operations of Bell–Shor algorithm are displayed in Figure 1b. The quantum states along the quantum circuit are denoted as ϕ_j $(j = 1, 2, ..., 5)$. The first register is linked to the cycle index of the C-Bell operations and it is adjustable by changing the number of controlling qubits to alter the periodic operations in the second one. While for the computing qubits in the second register, M_i is not limited by the quantum circuits for generating Bell states. It is also possible to increase the number to generate Greenberger-Horne-Zeilinger (GHZ) states [60] and W states [61] on more computing qubits. Furthermore, if M_i is set as the Grover iteration

G, the quasi-Shor algorithm would transform into an approximate quantum counting circuit [59].

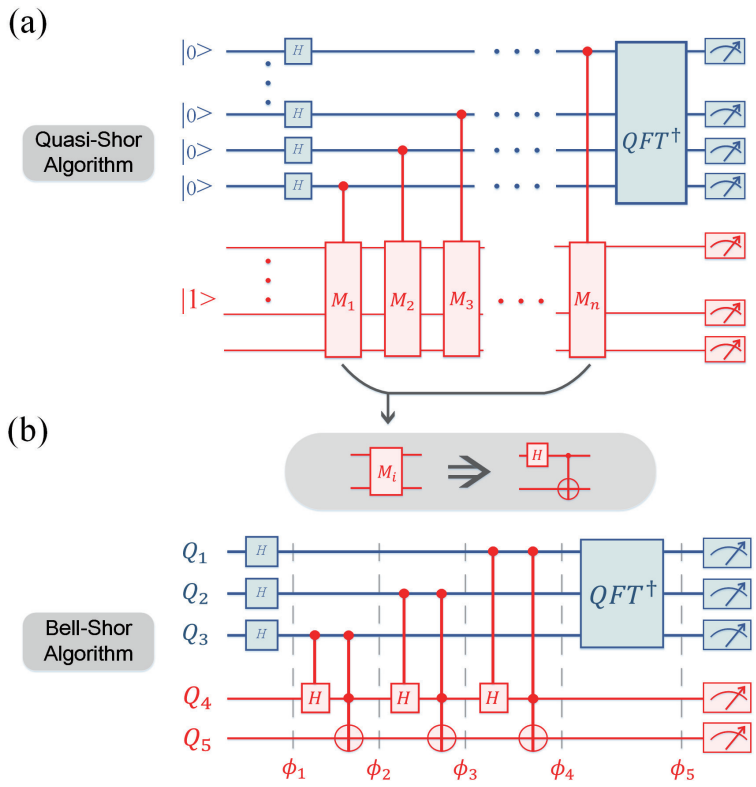


Figure 1. Schematic quantum circuit for quasi-Shor algorithms (**a**) and Bell–Shor algorithm (**b**).

3. Witness the Density Matrices

The initial states of the three controlling qubits and the two computing qubits are set as $|0\rangle^{\otimes 3}|00\rangle$. The quantum states $\phi_1, \phi_2, \phi_3, \phi_4$ are calculated analytically by matrices multiplications. To demonstrate the evolution of quantum states in Bell–Shor processing, Figure 2a–d display the density matrices $\rho_1, \rho_2, \rho_3, \rho_4$ corresponding to $\phi_1, \phi_2, \phi_3, \phi_4$, respectively. The elements marked with dark colors are zero (with accuracy $\leq 10^{-4}|E_{\max}|$, where $E_{\max}$ is the value of the element with the maximum absolute value). Running along the quantum circuit, it is noticeable that the states are becoming more complex and entangled. The zero elements are distributed as horizontal and vertical grids. The calculated results of the other three different input states $|01\rangle, |10\rangle, |11\rangle$ of computing qubits (i.e., the second register qubits) are shown in Appendix A.

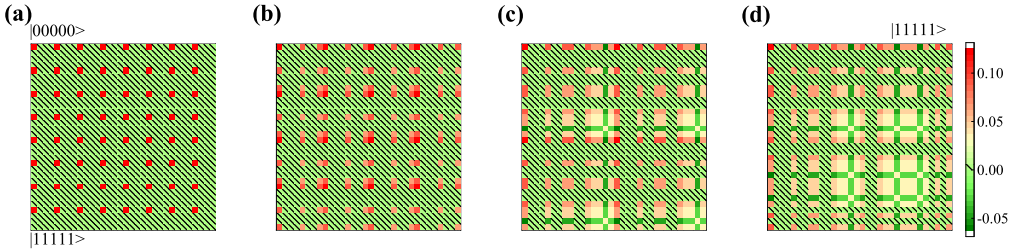


Figure 2. Density matrices for a series of quantum states during the processing ahead of $\mathrm{QFT}^\dagger$. (The input state is $|0\rangle^{\otimes 3}|00\rangle$). (**a**) The density matrix ρ_1 of ϕ_1. (**b**) The density matrix ρ_2 of ϕ_2. (**c**) The density matrix ρ_3 of ϕ_3. (**d**) The density matrix ρ_4 of ϕ_4.

Applying the $\mathrm{QFT}^\dagger$ operation to state ϕ_4, density matrices ρ_5 of ϕ_5 constructed with complex elements are shown in Figure 3. Here, the zero elements are marked with black color. In contrast to Figure 2, the translational symmetry of the grids is broken, whereas

local rotational symmetry emerges. The real parts of the density matrices remain symmetric about the main diagonal just as the density matrices before QFT†, and the elements in the main diagonal are all positive. The zero elements of the imaginary parts of the density matrices are also symmetric about the main diagonal, whereas the other elements are all conjugate with each other about the main diagonal. Moreover, the elements in the main diagonal are all zero. The number of zero elements in the real and imaginary parts are counted for in each quantum state.

Denoting the number of zero elements as n, the ratio $n/1024$ as a function of the quantum circuit depth is illustrated in Figure 4. The ratio is decreasing during the whole process. At first, 93.75% of the 1024 elements are zero, then with the operations of C-Bell and QFT†, n decreases to 16–20 finally. The zero elements drop to just a few dark points in the real density matrices and generate imaginary parts after the operation of QFT†.

In Table 1, the coordinates of the maximum elements and zero elements in the real parts of density matrices ρ_5 are listed specifically. There are obvious distinctions among these four input states. Designating $|00000\rangle\langle 00000|$ as (1,1) and $|11111\rangle\langle 11111|$ as (32,32), the coordinate of the maximum is (1,1) for both $|0\rangle^{\otimes 3}|00\rangle$ and $|0\rangle^{\otimes 3}|10\rangle$, while (2,2) for $|0\rangle^{\otimes 3}|01\rangle$ and $|0\rangle^{\otimes 3}|11\rangle$. The landscapes of these density matrices are spectacular with remarkable features. For the zero entries, there are about 16–20 elements with unique distributions for different input cases. In contrast to the real parts, the imaginary parts have a lot of zero entries and most are degenerated for different input states, i.e., the patterns of zero entries are nearly identical. Appendix A presents calculations of the reduced density matrices and the coordinates of the maximum element and zero entries.

Table 1. Coordinates of elements with the maximum and zero values in the real part of density matrices for the four input states. Designate $|00000\rangle\langle 00000|$ as (1,1) and $|11111\rangle\langle 11111|$ as (32,32).

Input States	$\|E\|_{max}$	Absolute Zero
$\|0\rangle^{\otimes 3}\|00\rangle$	(1,1)	(6,24);(7,25);(7,26);(9,23); (9,31);(10,23);(10,31);(15,25); (15,26);(16,30);(23,9);(23,10); (24,6);(25,7);(25,15);(26,7); (26,15);(30,16);(31,9);(31,10)
$\|0\rangle^{\otimes 3}\|01\rangle$	(2,2)	(5,23);(8,25);(8,26);(9,24); (9,32);(10,24);(10,32);(15,29); (16,25);(16,26);(23,5);(24,9); (24,10);(25,8);(25,16);(26,8); (26,16);(29,15);(32,9);(32,10)
$\|0\rangle^{\otimes 3}\|10\rangle$	(1,1)	(6,27);(6,28);(11,22);(11,30); (12,22);(12,30);(14,27);(14,28); (22,11);(22,12);(27,6);(27,14); (28,6);(28,14);(30,11);(30,12)
$\|0\rangle^{\otimes 3}\|11\rangle$	(2,2)	(5,27);(5,28);(11,21);(11,29); (12,21);(12,29);(13,27);(13,28); (27,5);(28,5);(21,12);(21,11); (29,11);(29,12);(27,13);(28,13)

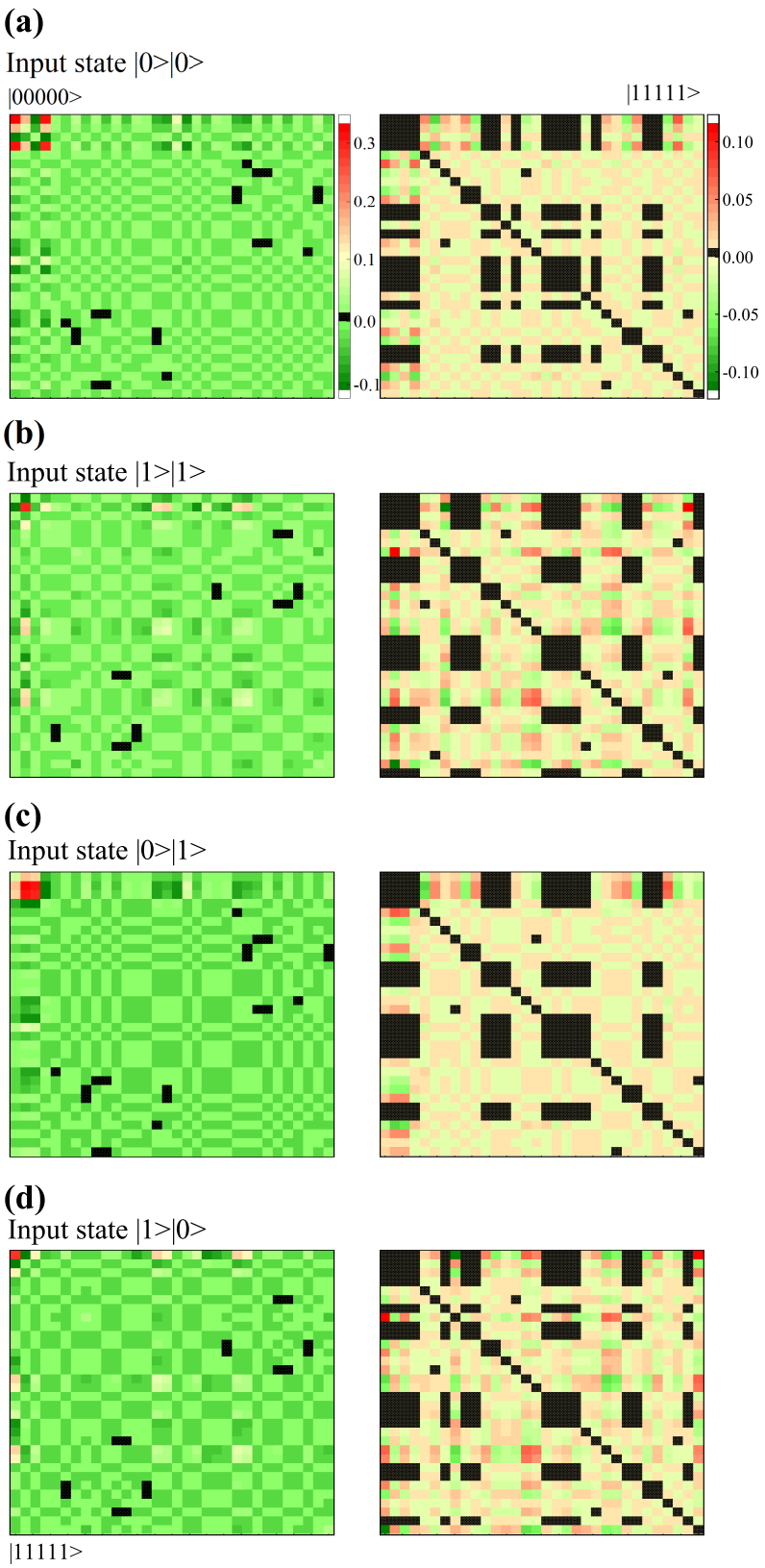


Figure 3. Density matrices ρ_5 for four distinct input states. The input state is $|0\rangle^{\otimes 3}|00\rangle$ (**a**), $|0\rangle^{\otimes 3}|01\rangle$ (**b**), $|0\rangle^{\otimes 3}|10\rangle$ (**c**), $|0\rangle^{\otimes 3}|11\rangle$ (**d**). Left panels are the real parts, while the right panels are the imaginary parts.

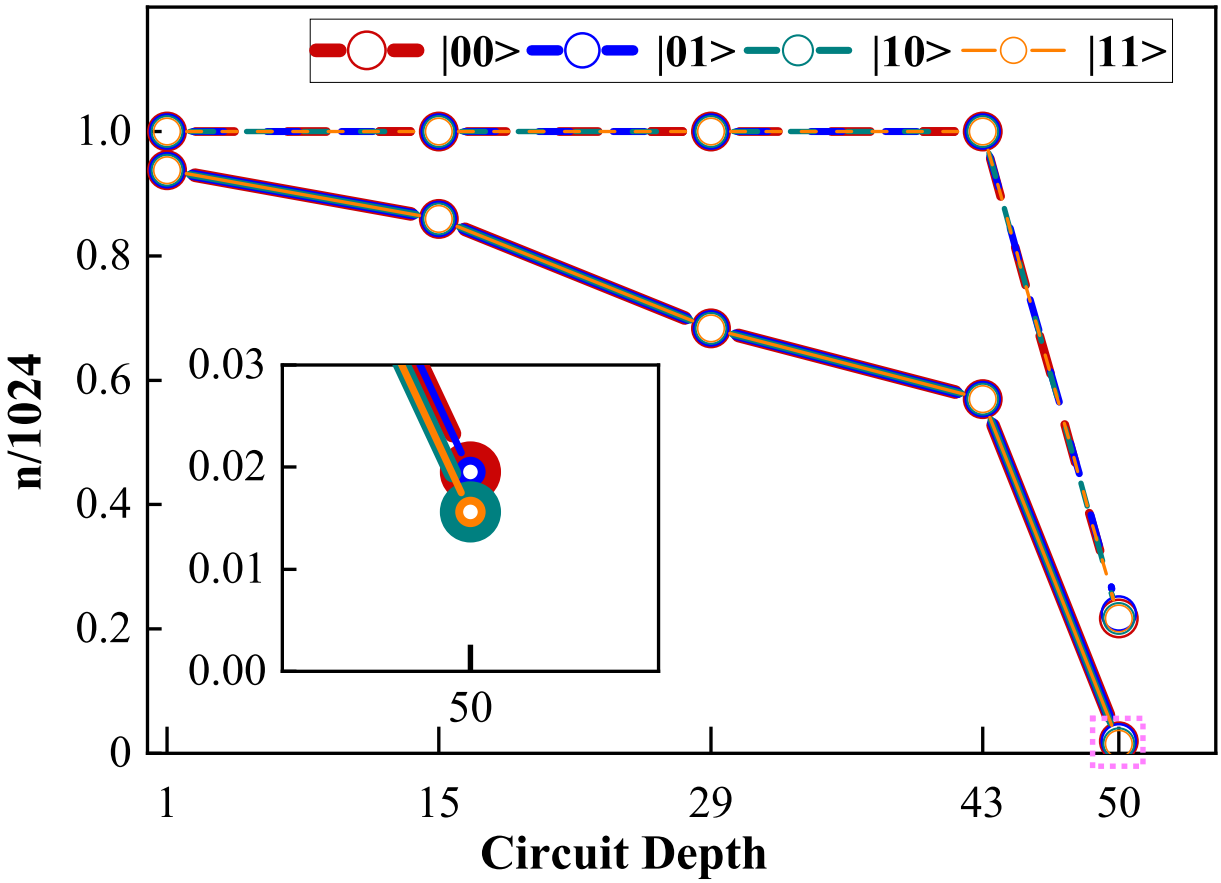


Figure 4. The ratio of the number of zero elements in the real part (solid lines) and that in the imaginary part (dashed lines) as a function of the quantum circuit depth. The inset presents the ratio of the final states after QFT†.

4. Error Metrics for Benchmarking

Now, the coordinates of the maximum and the zero elements in the density matrices could be utilized as a set of traits for global benchmarking of universal quantum processors by comparing the measured result with calculated ones. Defining the measured value of the dark points as P_i $(i = 1, 2, ..., n)$, the measured maximum as P_m according to the coordinates obtained from theoretical values, an error metric Γ_a of benchmarking is tentatively written as

$$\Gamma_a = \begin{cases} \text{Fail} & (P_m = 0) \\ 10\,\lg\left(\frac{\sum_{i=1}^{n}|P_i|}{n|P_m|}\right) & (P_m \neq 0), \end{cases} \tag{2}$$

which provides information about the inaccuracy of operations on the quantum processor. Here, the traits of output states depend on the input states and the fidelity of operations.

In Figure 5a, four states, including $|0\rangle^{\otimes 3}|00\rangle$, $|0\rangle^{\otimes 3}|01\rangle$, $|0\rangle^{\otimes 3}|10\rangle$, $|0\rangle^{\otimes 3}|11\rangle$ are utilized as tools to benchmark those with different states (e.g., $|000\rangle$, $|001\rangle$, . . ., $|111\rangle$) in the first register. It is obvious that the Γ_a is about –180 when using a few traits to benchmark themselves, while it becomes larger with the change in the first three states. Although Γ_a is reasonable and quite sensitive in most cases and has a complexity about $n + 1$, the fluctuations at some states (e.g., $|100\rangle|10\rangle$ and $|100\rangle|11\rangle$) are too large to be acceptable.

To enhance the robustness of the error metric, the completeness of the second register states is taken into consideration. Then another error metric Γ_b is constructed:

$$\Gamma_b = \begin{cases} \text{Fail} & (P_m = 0) \\ 10\lg(10^3 \frac{\sum_{j=1}^{4}\sum_{i=1}^{n_j}|P_i - P_{i_0}|}{n_{\text{tot}}|P_m|} + 1) & (P_m \neq 0), \end{cases} \tag{3}$$

where n_j is the number of zero elements in the jth calculated density matrix, n_{tot} is the total number of zero elements in the theoretical calculation, P_i (P_{i_0}) is the measured (ideal) value in the position of the ith element, and P_m is the measured value in the position of the maximum element. To enhance the sensitivity of Γ_b, a scaling factor of 10^3 is applied, and the addend constant 1 acts as a calibration term to ensure that the lower bound of Γ_b is zero.

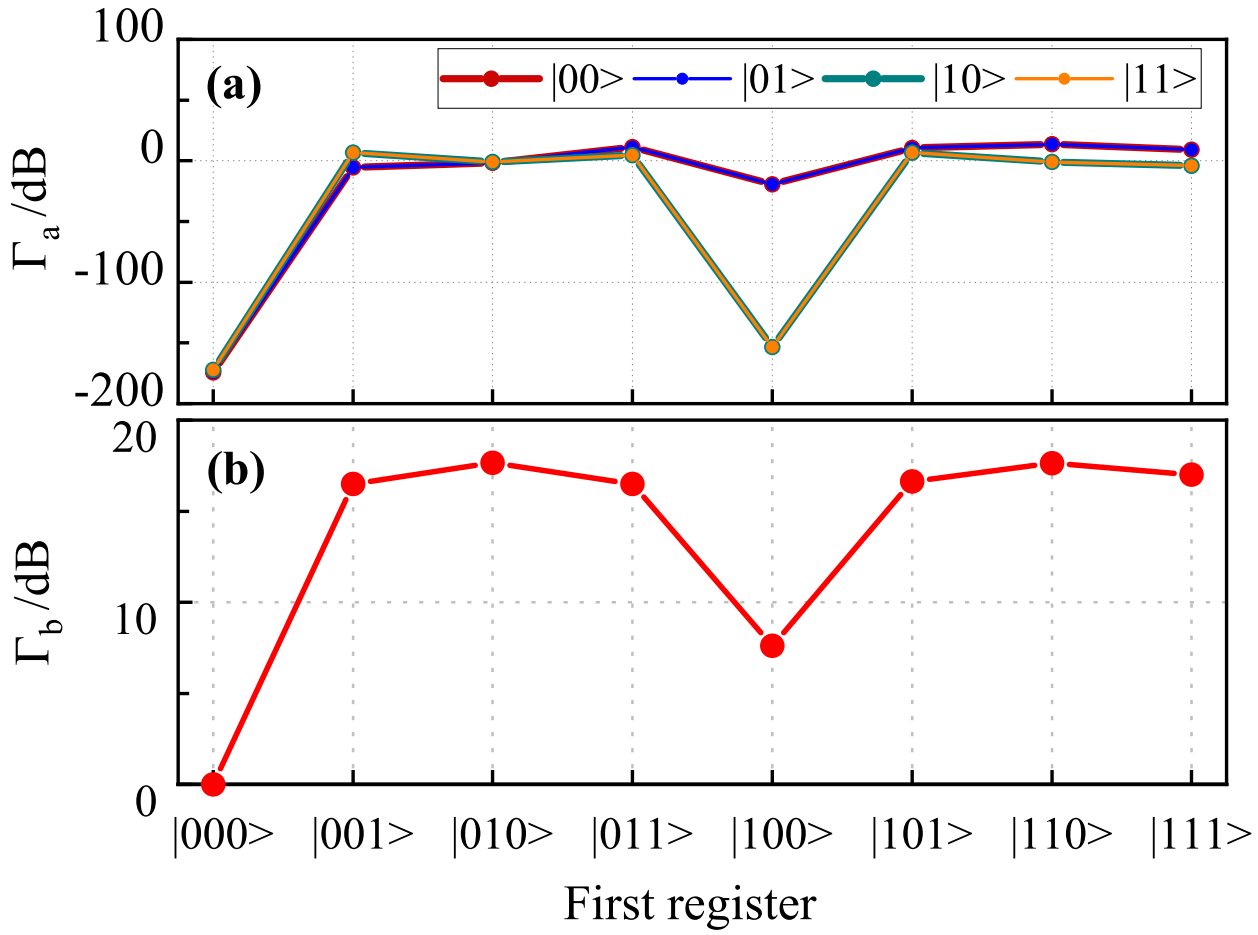


Figure 5. The results of benchmarking with error metrics Γ_a and Γ_b. (**a**) Γ_a uses $|0\rangle^{\otimes 3}|00\rangle$ (red line), $|0\rangle^{\otimes 3}|01\rangle$ (blue line), $|0\rangle^{\otimes 3}|10\rangle$ (green line), $|0\rangle^{\otimes 3}|11\rangle$ (purple line) as tools to benchmark these with different states in the first register, respectively. (**b**) Γ_b uses the state $|0\rangle^{\otimes 3}|00\rangle$, which combines the position of zero value in $|0\rangle^{\otimes 3}|01\rangle$, $|0\rangle^{\otimes 3}|10\rangle$ and $|0\rangle^{\otimes 3}|11\rangle$ together, and benchmark these states with the difference in the first register.

Figure 5b gives the benchmarking results of a series of states via utilizing the first register state $|000\rangle$, which has the complexity as $4n + 1$. Γ_b improves the robustness of the error metric via the completeness of the second register. It employs the locations of zero entries in the four kinds of input states and mitigates the influence of state preparation errors to some extent. The fluctuations are suppressed efficiently in comparison with Γ_a in Figure 5a.

To turn an empirical value into an interpretation of the performance of a quantum processor, it is helpful to examine the formula of Γ_b in some detail. In an ideal condition, one has $P_m \neq 0$ and $|P_i - P_{i_0}| = 0$, and this yields $\Gamma_b = 0$. While in practice, the value P_m in the location of the maximum according to the calculated result P_{m_0} is checked first. If $P_m = 0$, it means the quantum processor is failed. For $P_m \neq 0$, it is usually less than the calculated value P_{m_0}, and $|P_i - P_{i_0}|$ is larger than zero, therefore $\Gamma_b > 0$. This indicates the monotonic increase of Γ_b with noise.

Based on the above calculations, a global benchmarking protocol for universal quantum processors is introduced as follows:

1. For an N-qubit quantum processor, choose five qubits randomly;
2. Run the Bell–Shor algorithm on the five qubits;
3. Carry out state tomography for the final state;
4. Construct density matrices of the final state;
5. Look up Table 1 for the coordinates of the required entries;
6. Calculate two metrics Γ_a and Γ_b.

For the remaining $N - 5$ qubits, there are at least three feasible treatments:

(1) Leave the remaining $N - 5$ qubits in idle states when running the Bell–Shor algorithm on the five qubits. In this situation, it is important to move a certain number of frequencies of those $N - 5$ qubits away from the work frequency to reduce the disturbance on working qubits.

(2) Initialize and keep the remaining $N - 5$ qubits in the ground state. Because no other driving signal is applied to the $N - 5$ qubits, less resonance or entanglement would be generated among the selected five qubits to other qubits.

(3) Try to conduct parallel operations on a multi-group of five (or other) qubits. The advantage of this method is the high benchmarking efficiency, nevertheless, more control and readout lines are needed.

For the state tomography [59], measure $\langle \sigma_{v_1} \otimes \sigma_{v_2} \otimes \sigma_{v_3} \otimes \sigma_{v_4} \otimes \sigma_{v_5} \rangle$, where $\sigma_{v_i} (i = 1, 2, ..., 5)$ are chosen from the set of Pauli matrices $\sigma_0, \sigma_1, \sigma_2, \sigma_3$. The density matrices are reconstructed by

$$\rho = \sum_{\vec{v}} \frac{\mathrm{tr}(\sigma_{v_1} \otimes \sigma_{v_2} \otimes ... \otimes \sigma_{v_5} \rho) \sigma_{v_1} \otimes \sigma_{v_2} \otimes ... \otimes \sigma_{v_5}}{2^5}. \tag{4}$$

An alternative method for state tomography and reconstructing density matrices has been demonstrated by Reed, et al [62,63].

The Bell–Shor algorithm can be extended to a reasonably larger number of qubits, e.g., five to eight qubits. Here, a subset of k qubits with $2^k \times 2^k$ density matrices is used to benchmark the N-qubit quantum processor. The total number of selections could be counted as:

$$C_N^k = \frac{N!}{k!(N-k)!} < \frac{N^k}{k!}, (k = 5, 6, 7, 8). \tag{5}$$

Then the number of elements in the density matrices for the 5-qubit Bell–Shor algorithm is:

$$\frac{N!}{5!(N-5)!} \times 32^2 < \frac{N^5}{5!} \times 32^2 = \frac{N^5}{120} \times 32^2 = 8.53\ N^5, \tag{6}$$

which has polynomial scalability. Comparing with benchmarking N-qubit directly by $2^N \times 2^N$ density matrices, the total number of elements is 4^N, which scales exponentially.

As listed in Table 2, the number k of the calculating qubits is increased to study the change in the number $(\sum_{j=1}^{4} n_j)$ of zero elements. It could be seen that the total number of elements grows exponentially with k. However, the percentage of the number of zero elements keeps relatively steady except in the 6-qubit case, where an abnormal increase occurs. There is a trade-off between the choice of the qubit numbers k and the percentage of zero elements. The large sizes of elements would increase the calculation complexity, while too small qubit numbers would destroy the integrity of quasi-Shor algorithm.

Table 2. The change in the number of zero elements with an increase in the number of calculating qubits.

Number of Qubits k	Total Number of Elements 4×4^k	Total Number of Zero Elements $\sum_{j=1}^{4} n_j$	Percentage (%)
5	4×1024	72	1.758
6	4×4096	1520	9.277
7	$4 \times 16{,}384$	1096	1.672
8	$4 \times 65{,}536$	1916	0.731

Based on the information mentioned in Table 2, the locations of these special entries are shown in Figure 6, including all the zero entries in the four final density matrices with the following different initial states $|0\rangle^{\otimes k-2}|00\rangle$, $|0\rangle^{\otimes k-2}|01\rangle$, $|0\rangle^{\otimes k-2}|10\rangle$, and $|0\rangle^{\otimes k-2}|11\rangle$ ($k = 5, 6, 7, 8$). It could be seen that though the number of special elements in the 6-qubit case is abnormally larger than the others, and the distribution of zero entries has a spectacular cross "+" feature. Moreover, all these special points keep some characteristics of symmetry. For $k = 6, 7, 8$, the real part of the final density matrices (see Figure A3) are presented in Appendix B, where the application of Γ_b is also given (see Figure A4). A comparison of the number of elements among different k to the QST reveals that the present Bell–Shor global benchmarking protocol is polynomial to N (see Figure A5 in Appendix B).

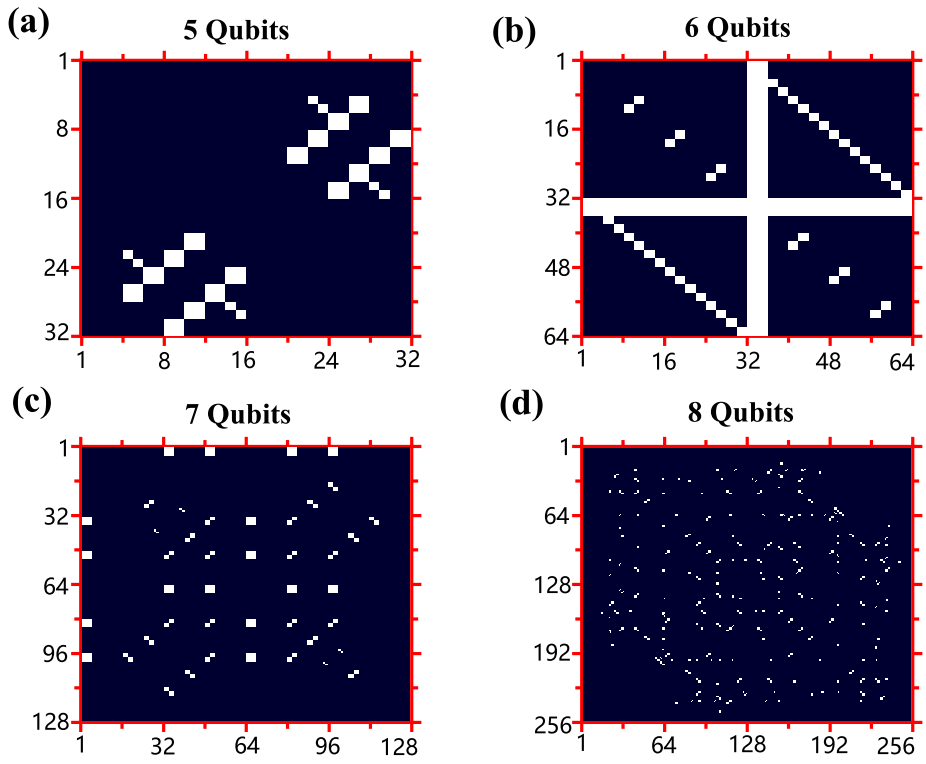


Figure 6. The locations of special entries are marked in the density matrices. (**a**) Example of 5 qubits. (**b**) Example of 6 qubits. (**c**) Example of 7 qubits. (**d**) Example of 8 qubits.

At this point, a comparison between the present benchmarking protocol with other approaches is necessary. The trend of Γ_b is compared with 1-Fidelity, state-Fidelity, and trace distance by calculation [59] and simulation in Qiskit [64] in Appendix C. In fact, the existing benchmarking approaches are mainly for single-qubit gates and two-qubit gates [47,53,54,56,57], which focus on the properties of qubits and might lack an emphasis on the interconnection among all the qubits in the processors. So here comes up a moderately sized algorithm for the global benchmarking of the architecture

of universal quantum processors, including the number and the interconnectivity of these qubits, as well as the computational depth of quantum circuits. The connection among qubits could be manifested through the entanglement generated among different qubits [65–68]. For more straightforward calculations, a quantum circuit for generating Bell states is taken as a specific example to construct the Bell–Shor algorithm on a subset of k qubits. This algorithm involves not only single-qubit operations on all these k qubits but also two-qubit operations between any two qubits, thus ensuring a benchmark of the universality of quantum processors.

5. Conclusions

In summary, this work proposes quasi-Shor algorithms, which share a similar framework with Shor's algorithm and also demand moderate requirements for the performance of quantum processors. It simplifies quantum operations by replacing the modular exponentiation component with a series of controlled-unitary operations. One variant of the quasi-Shor algorithm involves utilizing the controlled Bell-state preparations and construct the Bell–Shor algorithm. Density matrices along the quantum circuit are calculated and visualized. Remarkably, it is revealed that the number of zero elements decreases from 960 to only a few points in the real part of the density matrices after the inverse quantum Fourier transformation. Based on this property, a pair of error metrics (Γ_a and Γ_b) with polynomial increases are defined and the robustness is analyzed for various instances. A systematical benchmarking protocol for quantum processors is formulated with the two error metrics playing key roles. The proposed benchmarking protocol uses quantum state tomography to estimate the resulting density matrices of the final quantum states. The protocol then calculates the benchmarking metric by looking at the locations of the zero entries and normalized average values of non-zero entries. Bell–Shor global benchmarking protocol has polynomial scalability, which cuts down the exponential costs of full-state tomography, therefore, addressing the need for benchmarking the global performance of universal quantum processors. The rich physics contained in the quasi-Shor algorithms may accompany the research and development of universal quantum computers.

Author Contributions: Conceptualization, G.D. and J.L.; methodology, G.D.; software, G.D. and K.H.; validation, G.D., K.H. and J.L.; writing—original draft preparation, G.D.; writing—review and editing, G.D. and J.L.; supervision, C.Z., Y.H. and W.C.; project administration, W.C.; funding acquisition, W.C. All authors have read and agreed to the published version of the manuscript.

Funding: This work is supported by the National Natural Science Foundation of China (NSFC) grant nos. 60836001, 20161361354, and the Ministry of Science and Technology of the People's Republic of China (MOST) 973 program grant no. 2011CBA00304.

Data Availability Statement: All data generated or analyzed during this study are included in this published article.

Conflicts of Interest: No conflict of interest exists in the submission of this manuscript, and the manuscript was approved by all authors for publication. This work is original research that has not been published previously and is not under consideration for publication elsewhere, in whole or in part.

Appendix A. Visualization of Density Matrices

With the input state $|0\rangle^{\otimes 3}|00\rangle$, $|0\rangle^{\otimes 3}|01\rangle$, $|0\rangle^{\otimes 3}|10\rangle$, $|0\rangle^{\otimes 3}|11\rangle$; the density matrices during the processing are demonstrated in Figure A1.

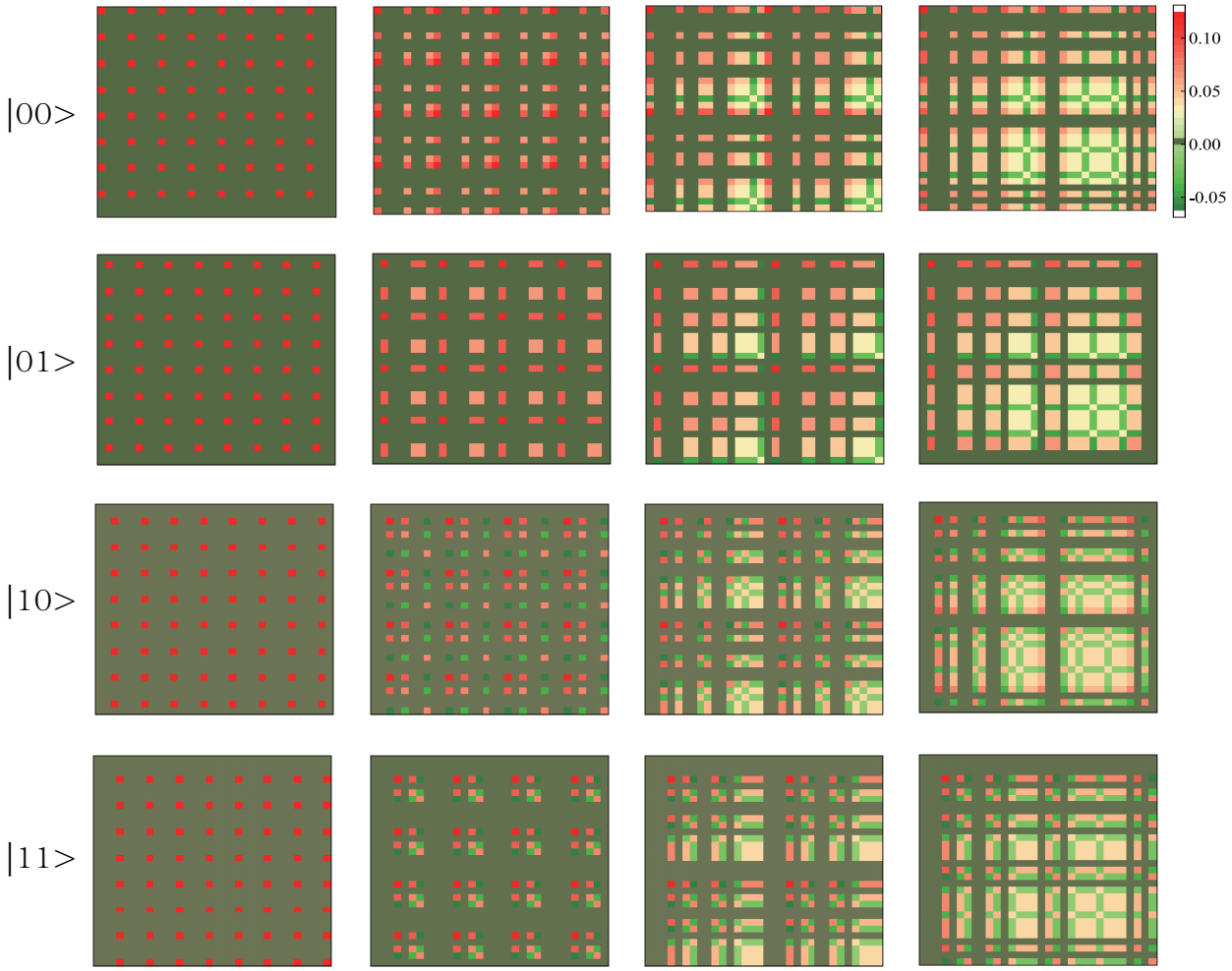


Figure A1. Density matrices of quantum states during the processing. Input states are $|0\rangle^{\otimes 3}|00\rangle$, $|0\rangle^{\otimes 3}|01\rangle$, $|0\rangle^{\otimes 3}|10\rangle$, and $|0\rangle^{\otimes 3}|11\rangle$. From the left to right are ρ_1, ρ_2, ρ_3, and ρ_4, respectively.

The two registers could be separated and their reduced density matrices are calculated by using partial trace over the register, which was not measured. This may help simplify the measurement process. The process satisfies the following equations [59]:

$$\rho^{A} \equiv \mathrm{Tr}_{B}(\rho^{AB}), \tag{A1}$$

$$\mathrm{Tr}_{B}(|a_1\rangle\langle a_2| \bigotimes |b_1\rangle\langle b_2|) \equiv |a_1\rangle\langle a_2|\mathrm{Tr}(|b_1\rangle\langle b_2|) \equiv |a_1\rangle\langle a_2|\langle b_2|b_1\rangle. \tag{A2}$$

Partial trace over the computing qubits mean just measuring the controlling qubits, while partial trace over the controlling qubits mean measuring the computing qubits.

As shown in Figure A2, the real parts of the density matrices are always symmetric concerning the main diagonal for the distinct input states, and the main diagonal of the imaginary part is zero. It could be seen that the four input states enjoy unique real parts of the reduced density matrices. In the imaginary part, there are some interesting features: it is the same between input states $|00\rangle$ and $|01\rangle$, as with $|10\rangle$ and $|11\rangle$ with partial tracing over the second register, while the results of the partial tracing over the first register are almost zero for all four input states. The coordinates of all elements with zero or the maximum values in these density matrices are gathered in Table A1.

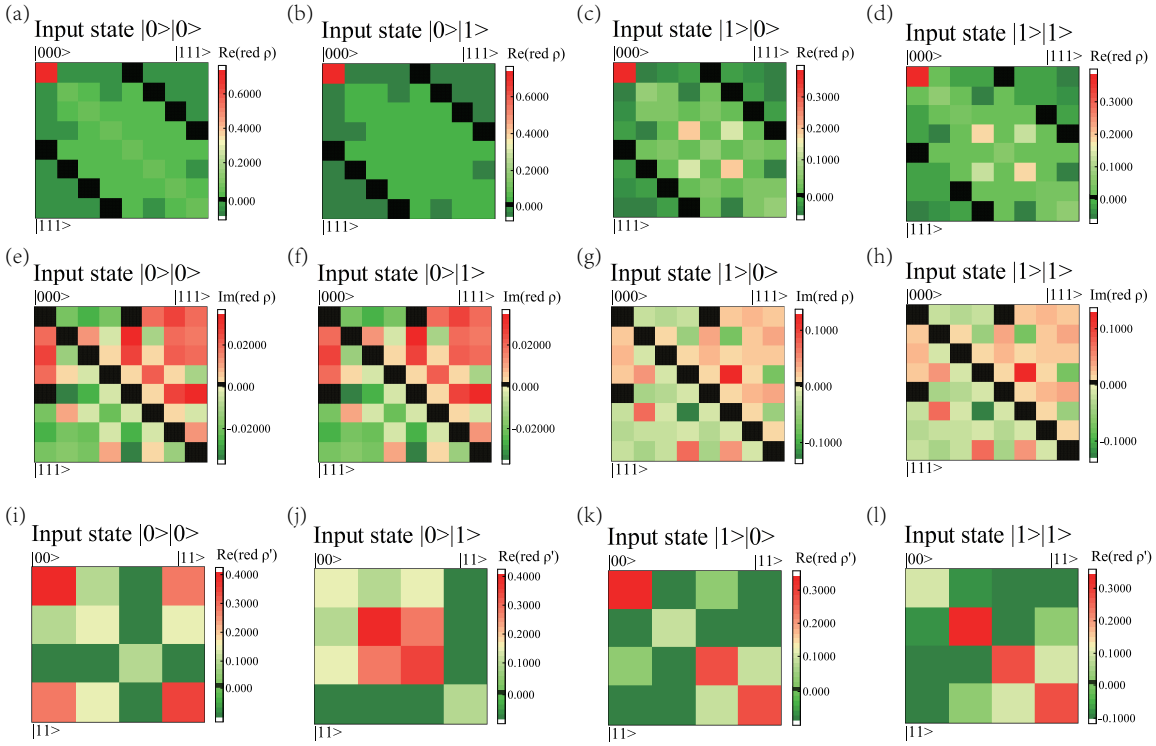


Figure A2. (**a**–**d**) The real parts of reduced density matrices of the first register. (**e**–**h**) The imaginary parts of reduced density matrices of the first register. (**i**–**l**) The real parts of reduced density matrices of the second register.

Table A1. Coordinates of elements with absolute zero values and maximum values in density matrices. Take the coordinates of element $|000\rangle\langle 000|$ ($|00\rangle\langle 00|$) in density matrices as (1,1) and $|111\rangle\langle 111|$ ($|11\rangle\langle 11|$) as (8,8) ((4,4)) for reduced density matrices over the second registers (the first registers).

Quantum States	Standard	Real Part	Imaginary Part
$\mathrm{Tr}_{\mathrm{II}}(\|0\rangle^{\otimes 3}\|0\rangle\|0\rangle)$	$\|E\|_{max}$ Absolute Zero	(1,1) (1,5);(2,6);(3,7);(4,8); (5,1);(6,2);(7,3);(8,4)	(2,5);(5,2);(5,8);(8,5) (1,1);(2,2);(3,3);(4,4);(5,5); (6,6);(7,7);(8,8);(1,5);(5,1)
$\mathrm{Tr}_{\mathrm{II}}(\|0\rangle^{\otimes 3}\|0\rangle\|1\rangle)$	$\|E\|_{max}$ Absolute Zero	(1,1) (1,5);(2,6);(3,7);(4,8); (5,1);(6,2);(7,3);(8,4)	(2,5);(5,2);(5,8);(8,5) (1,1);(2,2);(3,3);(4,4);(5,5); (6,6);(7,7);(8,8);(1,5);(5,1)
$\mathrm{Tr}_{\mathrm{II}}(\|0\rangle^{\otimes 3}\|1\rangle\|0\rangle)$	$\|E\|_{max}$ Absolute Zero	(1,1) (1,5);(2,6);(3,7);(4,8); (5,1);(6,2);(7,3);(8,4)	(6,4);(4,6) (1,1);(2,2);(3,3);(4,4);(5,5); (6,6);(7,7);(8,8);(1,5);(5,1)
$\mathrm{Tr}_{\mathrm{II}}(\|0\rangle^{\otimes 3}\|1\rangle\|1\rangle)$	$\|E\|_{max}$ Absolute Zero	(1,1) (1,5);(3,7);(4,8); (5,1);(7,3);(8,4)	(6,4);(4,6) (1,1);(2,2);(3,3);(4,4);(5,5); (6,6);(7,7);(8,8);(1,5);(5,1)
$\mathrm{Tr}_{\mathrm{I}}(\|0\rangle^{\otimes 3}\|0\rangle\|0\rangle)$	$\|E\|_{max}$ Absolute Zero	(1,1) None	None All
$\mathrm{Tr}_{\mathrm{I}}(\|0\rangle^{\otimes 3}\|0\rangle\|1\rangle)$	$\|E\|_{max}$ Absolute Zero	(2,2) None	None All
$\mathrm{Tr}_{\mathrm{I}}(\|0\rangle^{\otimes 3}\|1\rangle\|0\rangle)$	$\|E\|_{max}$ Absolute Zero	(1,1) None	None All
$\mathrm{Tr}_{\mathrm{I}}(\|0\rangle^{\otimes 3}\|1\rangle\|1\rangle)$	$\|E\|_{max}$ Absolute Zero	(2,2) None	(2,3);(3,2) (1,1);(1,3);(1,4);(2,2);(2,4);(3,1); (3,3);(3,4);(4,1);(4,2);(4,3);(4,4)

Appendix B. Bell–Shor Algorithm with Larger Numbers of Qubits

In Figure A3, the final density matrices for the Bell–Shor algorithm k = 6, 7, 8 are displayed with initial states $|0\rangle^{\otimes 6}$ (a), $|0\rangle^{\otimes 7}$ (b), and $|0\rangle^{\otimes 8}$ (c). Interestingly, the zero elements in Figure A3a form a key feature of cross "+" distribution. In the 8-qubit case, these special elements seem to have mirror symmetry concerning the counter-diagonal.

As depicted in Figure A4, it is clear that Γ_b keeps a similar trend with more qubits k. With the choice of the larger numbers of qubits $k(k = 6,7,8)$, there is an overall decline in the amplitude of Γ_b.

In Figure A5, the horizontal axis N is the number of qubits in the quantum processor, and the vertical axis N_{te} is the total number of elements, which is needed for the complete benchmarking. With the increase in the size of the quantum processor, the exponential growth of N_{te} could be cut down by introducing the Bell–Shor algorithm.

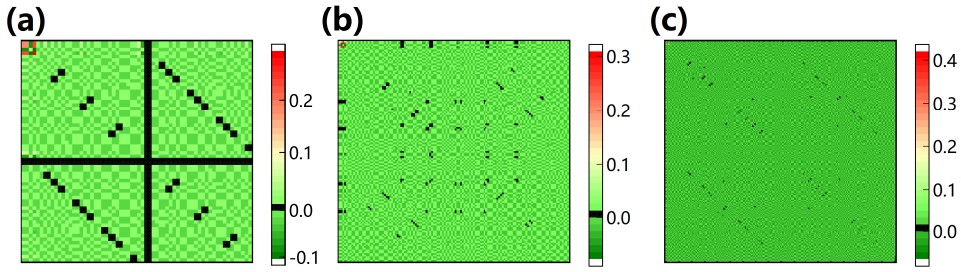


Figure A3. The real part of the final density matrices for $k = 6,7,8$ qubits. (**a**) The input state is $|0\rangle^{\otimes 6}$. (**b**) The input state is $|0\rangle^{\otimes 7}$. (**c**) The input state is $|0\rangle^{\otimes 8}$.

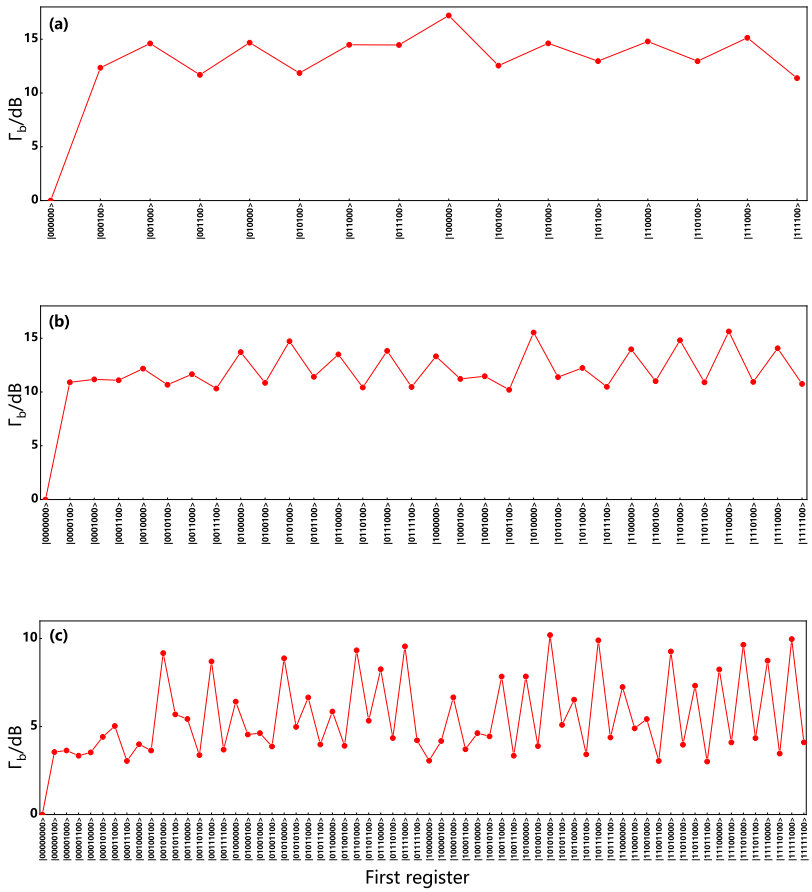


Figure A4. Calculation of Γ_b for $k = 6,7,8$ qubits. (**a**) The input state is $|0\rangle^{\otimes 6}$. (**b**) The input state is $|0\rangle^{\otimes 7}$. (**c**) The input state is $|0\rangle^{\otimes 8}$.

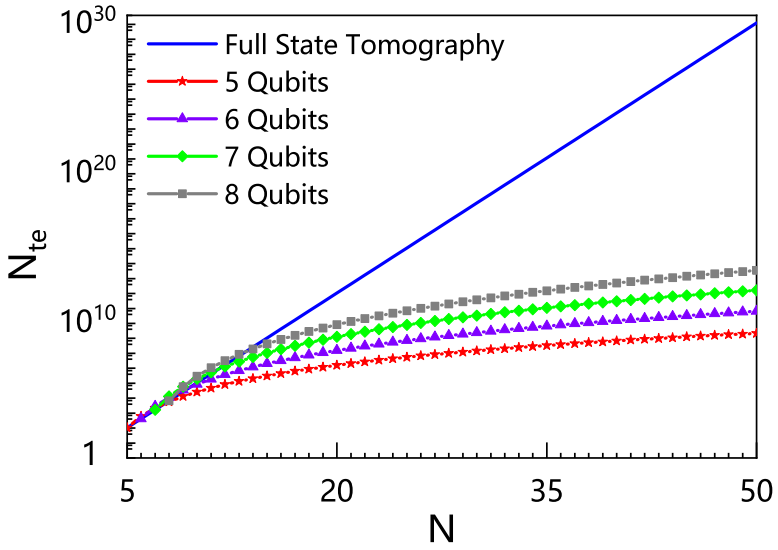


Figure A5. Comparison among the number of elements used in different methods, including full state tomography and the Bell–Shor algorithm on k qubits ($k = 5, 6, 7, 8$).

Appendix C. Calculation and Simulation of Γ_b and Fidelity

Here, we compare the trends of Γ_b with 1-fidelity F_1, state-fidelity F_s, and trace distance F_d, including calculation [59] and simulation in Qiskit [64]. The formulas of F_1, F_s, and F_d are as follows:

$$F_1 = ||\rho_0^{\frac{1}{2}} \rho^{\frac{1}{2}}||_1^2, \tag{A3}$$

$$F_s = \mathrm{Tr}(\rho\rho_0), \tag{A4}$$

$$F_d = \frac{1}{2}||\rho - \rho_0||_1, \tag{A5}$$

where ρ is the measured state, ρ_0 is the ideal state, and $||A||_1 = \mathrm{Tr}(\sqrt{A^\dagger A})$.

As shown in Figure A6, all four metrics are able to distinguish the eight states, while the differences become smaller in the simulator.

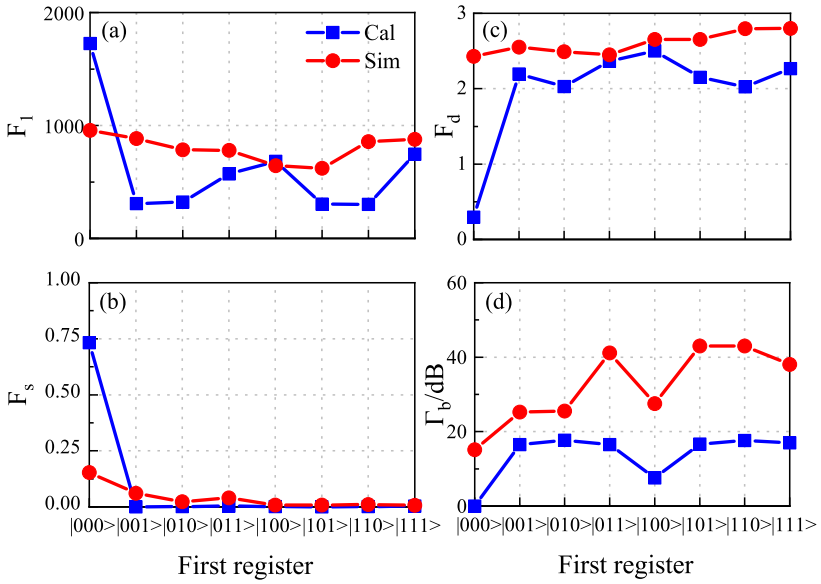


Figure A6. Comparison between the 1-fidelity F_1, state-fidelity F_s, and trace distance F_d with Γ_b. Blue curves represent the calculated results and the red curves are the simulated results by the "qasm simulator" in Qiskit.

References

1. Devoret, M.H.; Schoelkopf, R.J. Superconducting Circuits for Quantum Information: An Outlook. *Science* **2013**, *339*, 1169–1174. [CrossRef] [PubMed]
2. Rasmussen, S.; Christensen, K.; Pedersen, S.; Kristensen, L.; Bækkegaard, T.; Loft, N.; Zinner, N. Superconducting Circuit Companion—An Introduction with Worked Examples. *PRX Quantum* **2021**, *2*, 040204. [CrossRef]
3. Bruzewicz, C.D.; Chiaverini, J.; McConnell, R.; Sage, J.M. Trapped-ion quantum computing: Progress and challenges. *Appl. Phys. Rev.* **2019**, *6*, 021314. [CrossRef]
4. Wright, K.; Beck, K.M.; Debnath, S.; Amini, J.M.; Nam, Y.; Grzesiak, N.; Chen, J.-S.; Pisenti, N.C.; Chmielewski, M.; Collins, C.; et al. Benchmarking an 11-qubit quantum computer. *Nat. Commun.* **2019**, *10*, 5464. [CrossRef] [PubMed]
5. Zu, C.; Wang, W.-B.; He, L.; Zhang, W.-G.; Dai, C.-Y.; Wang, F.; Duan, L.-M. Experimental realization of universal geometric quantum gates with solid-state spins. *Nature* **2014**, *514*, 72–75. [CrossRef] [PubMed]
6. Lekitsch, B.; Weidt, S.; Fowler, A.G.; Mølmer, K.; Devitt, S.J.; Wunderlich, C.; Hensinger, W.K. Blueprint for a microwave trapped ion quantum computer. *Nature* **2017**, *3*, 2. [CrossRef]
7. Mong, R.S.K.; Clarke, D.J.; Alicea, J.; Lindner, N.H.; Fendley, P.; Nayak, C.; Oreg, Y.; Stern, A.; Berg, E.; Shtengel, K.; et al. Universal Topological Quantum Computation from a Superconductor-Abelian Quantum Hall Heterostructure. *Phys. Rev. X* **2014**, *4*, 011036. [CrossRef]
8. Terhal, B.M. Quantum error correction for quantum memories. *Rev. Mod. Phys.* **2015**, *87*, 307–346. [CrossRef]
9. Harrow, A.W.; Montanaro, A. Quantum computational supremacy. *Nature* **2017**, *549*, 203–209. [CrossRef]
10. Campbell, E.T.; Terhal, B.M.; Vuillot, C. Roads towards fault-tolerant universal quantum computation. *Nature* **2017**, *549*, 172–179. [CrossRef]
11. Moll, N.; Barkoutsos, P.; Bishop, L.S.; Chow, J.M.; Cross, A.; Egger, D.J.; Filipp, S.; Fuhrer, A.; Gambetta, J.M.; Ganzhorn, M.; et al. Quantum optimization using variational algorithms on near-term quantum devices. *Quantum Sci. Technol.* **2018**, *3*, 030503. [CrossRef]
12. Deutsch, D. Quantum theory, the Church-Turing principle and the universal quantum computer. *Proc. R. Soc. Lond. A* **1985**, *400*, 97–117.
13. Deutsch, D.; Jozsa, R. Rapid solution of problems by quantum computation. *Math. Phys. Eng. Sci.* **1992**, *439*, 553–558.
14. DiCarlo, L.; Chow, J.M.; Gambetta, J.M.; Bishop, L.S.; Johnson, B.R.; Schuster, D.I.; Majer, J.; Blais, A.; Frunzio, L.; Girvin, S.M.; et al. Demonstration of two-qubit algorithms with a superconducting quantum processor. *Nature* **2009**, *460*, 240–244. [CrossRef]
15. Sangskriti, S.; Nag, P.; Haque, S. Fundamental Machine Learning Routines as Quantum Algorithms on a Superconducting Quantum Computer. *arXiv* **2021**, arXiv:2109.09522.
16. Lee, Y.; Joo, J.; Lee, S. Hybrid quantum linear equation algorithm and its experimental test on IBM Quantum Experience. *Sci. Rep.* **2019**, *9*, 4778. [CrossRef] [PubMed]
17. Harrow, A.W.; Hassidim, A.; Lloyd, S. Quantum Algorithm for Linear Systems of Equations. *Phys. Rev. Lett.* **2009**, *103*, 150502. [CrossRef]
18. Chen, C.-C.; Shiau, S.-Y.; Wu, M.-F.; Wu, Y.-R. Hybrid classical-quantum linear solver using Noisy Intermediate-Scale Quantum machines. *Sci. Rep.* **2019**, *9*, 16251. [CrossRef]
19. Shor, P.W. Polynomial-Time Algorithms for Prime Factorization and Discrete Logarithms on a Quantum Logarithms on a Quantum Computer. *Siam J. Comput.* **1997**, *26*, 1484–1509. [CrossRef]
20. Skosana, U.; Tame, M. Demonstration of Shor's factoring algorithm for N = 21 on IBM quantum processors. *Sci. Rep.* **2021**, *11*, 16599. [CrossRef]
21. Figgatt, C.; Maslov, D.; Landsman, K.; Linke, N.M.; Debnath, S.; Monroe, C.R. Complete 3-Qubit Grover search on a programmable quantum computer. *Nat. Commun.* **2017**, *8*,1918. [CrossRef] [PubMed]
22. Damm, W.V.; Hayden, P. Universal entanglement transformations without communication. *Phys. Rev. A* **2003**, *67*, 060302.
23. Zhou, X.-Q.; Kalasuwan, P.; Ralph, T.; O'Brien, J. Calculating unknown eigenvalues with a quantum algorithm. *Nat. Photon.* **2013**, *7*, 223–228. [CrossRef]
24. Vandersypen, L.M.K.; Steffen, M.; Breyta, G.; Yannoni, C.S.; Sherwood, M.H.; Chuang, I.L. Experimental realization of Shor's quantum factoring algorithm using nuclear magnetic resonance. *Nature* **2001**, *414*, 883–887. [CrossRef] [PubMed]
25. López, E.M.; Laing, A.; Lawson, T.; Alvarez, R.; Zhou, X.Q.; O'Biren, J.L. Experimental realization of Shor's quantum factoring algorithm using qubit recycling. *Nat. Photon.* **2012**, *6*, 773–776. [CrossRef]
26. Greganti, C.; Demarie, T.F.; Ringbauer, M.; Jones, J.A.; Saggio, V.; Calafell, I.A.; Rozema, L.A.; Erhard, A.; Meth, M.; Postler, L.; et al. Cross-verification of independent quantum devices. In Proceedings of the 2021 Conference on Lasers and Electro-Optics Europe & European Quantum Electronics Conference (CLEO/Europe-EQEC), Munich, Germany, 21–25 June 2021.
27. Chen, Y.-T.; Farquhar, C.; Parrish, R.M. Low-rank density-matrix evolution for noisy quantum circuits. *NPJ Quantum Inf.* **2021**, *7*, 61. [CrossRef]
28. Roulet, J.; Vanicek, J. An implicit split-operator algorithm for the nonlinear time-dependent Schrödinger equation. *J. Chem. Phys.* **2021**, *155*, 204109. [CrossRef]
29. Chen, R.; Zhao, B.; Wang, X. Variational Quantum Algorithm for Schmidt Decomposition. *arXiv* **2021**, arXiv:2109.10785v1.
30. Wang, B.; Hu, F.; Yao, H.; Wang, C. Prime factorization algorithm based on parameter optimization of Ising model. *Sci. Rep.* **2020**, *10*, 7106. [CrossRef]

31. Shor, P.W. Progress in Quantum Algorithms. In *Experimental Aspects of Quantum Computing*; Springer: Berlin/Heidelberg, Germany, 2007; pp. 5–13
32. He, Y.C.; Zhao, C.H.; Dai, G.T.; He, K.Y.; Geng, X.; Liu, J.S.; Chen, W. Quantum modular multiplier via binary-exponent-based recombination. *Quantum Inf. Process.* **2022**, *21*, 391. [CrossRef]
33. Ferraro, E.; Michielis, M.D. On the robustness of the hybrid qubit computational gates through simulated randomized benchmarking protocols. *Sci. Rep.* **2020**, *10*, 17780. [CrossRef] [PubMed]
34. Onorati, E.; Werner, A.H.; Eisert, J. Randomized Benchmarking for Individual Quantum Gates. *Phys. Rev. Lett.* **2019**, *123*, 060501. [CrossRef]
35. Benedetti, M.; Pintos, D.G.; Perdomo, O.; Ortega, V.L.; Nam, Y.; Ortiz, A.P. A generative modeling approach for benchmarking and training shallow quantum circuits. *Npj Quantum Inform.* **2019**, *5*, 45. [CrossRef]
36. Chasseur, T.; Reich, D.M.; Koch, C.; Wilhelm, F.K. Hybrid benchmarking of arbitrary quantum gates. *Phys. Rev. A* **2017**, *95*, 062335. [CrossRef]
37. Knill, E.; Leibfried, D.; Reichle, R.; Britton, J.; Blakestad, R.B.; Jost, J.D.; Langer, C.; Ozeri, R.; Seidelin, S.; Wineland, D.J. Randomized benchmarking of quantum gates. *Phys. Rev. A* **2008**, *77*, 012307. [CrossRef]
38. Huang, Y.-T.; Lin, J.-D.; Ku, H.-Y.; Chen, Y.-N. Benchmarking quantum state transfer on quantum devices. *Phys. Rev. Res.* **2021**, *3*, 023038. [CrossRef]
39. Yuan, X.; Liu, Y.; Zhao, Q.; Regula, B.; Thompson, J.; Gu, M. Universal and operational benchmarking of quantum memories. *NPJ Quantum Inf.* **2021**, *7*, 108. [CrossRef]
40. Eisert, J.; Hangleiter, D.; Walk, N.; Roth, I.; Markham, D.; Parekh, R.; Chabaud, U.; Kashefi, E. Quantum certification and benchmarking. *Nat. Rev. Phys.* **2020**, *2*, 382–390. [CrossRef]
41. Eisert, J.; Hangleiter, D.; Walk, N.; Roth, I.; Markham, D.; Parekh, R.; Chabaud, U.; Kashefi, E. Quantum benchmarking with realistic states of light. *Phys. Rev. A* **2012**, *86*, 022331.
42. Nakata, Y.; Zhao, D.; Okuda, T.; Bannai, E.; Suzuki, Y.; Tamiya, S.; Heya, K.; Yan, Z.G.; Zuo, K.; Tamate, S.H.; et al. Quantum Circuits for Exact Unitary t-Designs and Applications to Higher-Order Randomized Benchmarking. *PRX Quantum* **2021**, *2*, 030339. [CrossRef]
43. Subires, D.; Ruiz, F.J.G.; García, A.R.; Alonso, D.; Campo, A.D. Benchmarking quantum annealing dynamics: The spin-vector Langevin model. *Phys. Rev. Res.* **2022**, *4*, 023104. [CrossRef]
44. Song, C.; Cui, J.; Wang, H.; Hao, J.; Feng, H.; Li, Y. Quantum computation with universal error mitigation on a superconducting quantum processor. *Sci. Adv.* **2019**, *5*, 9. [CrossRef] [PubMed]
45. Erhard, A.; Wallman, J.J.; Postler, L.; Meth, M.; Stricker, R.; Martinez, E.A.; Schindler, P.; Monz, T.; Emerson, J.; Blatt, R. Characterizing large-scale quantum computers via cycle benchmarking. *Nat. Commun.* **2019**, *10*, 5347 [CrossRef] [PubMed]
46. Flamini, F.; Spagnolo, N.; Viggianiello, N.; Crespi, A.; Osellame, R.; Sciarrino, F. Benchmarking integrated linear-optical architectures for quantum information processing. *Sci. Rep.* **2017**, *7*, 15133. [CrossRef]
47. Magesan, E.; Gambetta, J.M.; Emerson, J. Scalable and Robust Randomized Benchmarking of Quantum Processes. *Phys. Rev. Lett.* **2011**, *106*, 180504. [CrossRef]
48. Knill, E.; Laflamme, R.; Martinez, R.; Negrevergne, C. Benchmarking Quantum Computers: The Five-Qubit Error Correcting Code. *Phys. Rev. Lett.* **2001**, *86*, 5811–5814. [CrossRef]
49. Knill, E.; Laflamme, R.; Martinez, R.; Negrevergne, C. Sampling Strategy Optimization for Randomized Benchmarking. *arXiv* **2019**, arXiv:2109.07653.
50. Grant, E.; Humble, T.S.; Stump, B. Benchmarking Quantum Annealing Controls with Portfolio Optimization. *Phys. Rev. Appl.* **2021**, *15*, 014012. [CrossRef]
51. Regula, B.; Bu, K.; Takagi, R.; Liu, Z.-W. Benchmarking one-shot distillation in general quantum resource theories. *Phys. Rev. A* **2020**, *101*, 062315. [CrossRef]
52. Lathiotakis, N.N.; Marques, M.A.L. *Benchmark calculations for reduced density-matrix functional theory*. *J. Chem. Phys.* **2008**, *128*, 184103. [CrossRef]
53. Arute, F.; Arya, K.; Babbush, R.; Bacon, D.; Bardin, J.C.; Barends, R.; Biswas, R.; Boixo, S.; Brandao, F.G.S.L.; Buell, D.A.; et al. Quantum supremacy using a programmable superconducting processor. *Nature* **2019**, *574*, 505–510. [CrossRef] [PubMed]
54. Wu, Y.L.; Bao, W.S.; Cao, S.R.; Chen, F.S.; Chen, M.C.; Chen, X.W.; Chung, T.H.; Deng, H.; Du, Y.J.; Fan, D.J.; et al. Benchmark calculations for reduced density-matrix functional theory. *Phys. Rev. Lett.* **2021**, *127*, 180501. [CrossRef] [PubMed]
55. Jafferis, D.; Zlokapa, A.; Lykken, J.D.; Kolchmeyer, D.K.; Davis, S.I.; Lauk, N.; Neven, H.; Spiropulu, M. Traversable wormhole dynamics on a quantum processor. *Nature* **2022**, *612*, 51–55. [CrossRef]
56. Corcoles, A.D.; Gambetta, J.M.; Chow, J.M.; Smolin, J.A.; Ware, M.; Strand, J.; Plourde, B.L.; Steffen, M. Process verification of two-qubit quantum gates by randomized benchmarking. *Phys. Rev. A* **2013**, *87*, 030301. [CrossRef]
57. Barends, R.; Kelly, J.; Megrant, A.; Veitia, A.; Sank, D.; Jeffrey, E.; White, T.; Mutus, J.; Fowler, A.; Campbell, B.; et al. Superconducting quantum circuits at the surface code threshold for fault tolerance. *Nature* **2014**, *508*, 500–503. [CrossRef] [PubMed]
58. Song, C.; Xu, K.; Liu, W.; Yang, C.-P.; Zheng, S.-B.; Deng, H.; Xie, Q.; Huang, K.; Guo, Q.; Zhang, L.; et al. 10-Qubit Entanglement and Parallel Logic Operations with a Superconducting Circuit. *Phys. Rev. Lett.* **2017**, *119*, 180511. [CrossRef] [PubMed]
59. Nielsen, M.A.; Chuang, I.; Grover, L.K. Quantum Computation and Quantum Information. *Am. J. Phys.* **2002**, *70*, 558–559. [CrossRef]

60. Erhard, M.; Malik, M.; Krenn, M.; Zeilinger, A. Experimental Greenberger–Horne–Zeilinger entanglement beyond qubits. *Nat. Photon.* **2018**, *12*, 759–764. [CrossRef]
61. Dür, W.; Vidal, G.; Cirac, J.I. Three qubits can be entangled in two inequivalent ways. *Phys. Rev. A* **2000**, *62*, 062314. [CrossRef]
62. Reed, M.D.; DiCarlo, L.; Nigg, S.E.; Sun, L.; Frunzio, L.; Girvin, S.M.; Schoelkopf, R.J. Realization of three-qubit quantum error correction with superconducting circuits. *Nature* **2012**, *482*, 382–385. [CrossRef]
63. Reed, M.D. Entanglement and Quantum Error Correction with Superconducting Qubits. *arXiv* **2013**, arXiv:1311.6759v1.
64. Available online: https://qiskit.org/ (accessed on 30 May 2021).
65. Vedral, V.; Plenio, M.B.; Rippin, M.A.; Knight, P.L. Quantifying Entanglement. *Phys. Rev. Lett.* **1997**, *78*, 2275–2279. [CrossRef]
66. Wei, T.-C.; Goldbart, P.M. Geometric measure of entanglement and applications to bipartite and multipartite quantum states. *Phys. Rev. A* **2003**, *68*, 042307. [CrossRef]
67. Amico, L.; Fazio, R.; Osterloh, A.; Vedral, V. Entanglement in many-body systems. *Rev. Mod. Phys.* **2008**, *80*, 517–576. [CrossRef]
68. Bennett, C.H.; Bernstein, H.J.; Popescu, S.; Schumacher, B. Concentrating partial entanglement by local operations. *Phys. Rev. A* **1996**, *53*, 2046–2052. [CrossRef] [PubMed]

Disclaimer/Publisher's Note: The statements, opinions and data contained in all publications are solely those of the individual author(s) and contributor(s) and not of MDPI and/or the editor(s). MDPI and/or the editor(s) disclaim responsibility for any injury to people or property resulting from any ideas, methods, instructions or products referred to in the content.